

## Editor's Choice

# One-step construction of a transition-metal surface decorated with metal sulfide nanoparticles: A high-efficiency electrocatalyst for hydrogen generation



Yulin Sun <sup>a,1</sup>, Chuanqi Huang <sup>b,1</sup>, Junling Shen <sup>a,1</sup>, Yijun Zhong <sup>a,\*</sup>, Jiqiang Ning <sup>c</sup>, Yong Hu <sup>a,\*</sup>

<sup>a</sup> Key Laboratory of the Ministry of Education for Advanced Catalysis Materials, Department of Chemistry, Zhejiang Normal University, Jinhua 321004, China

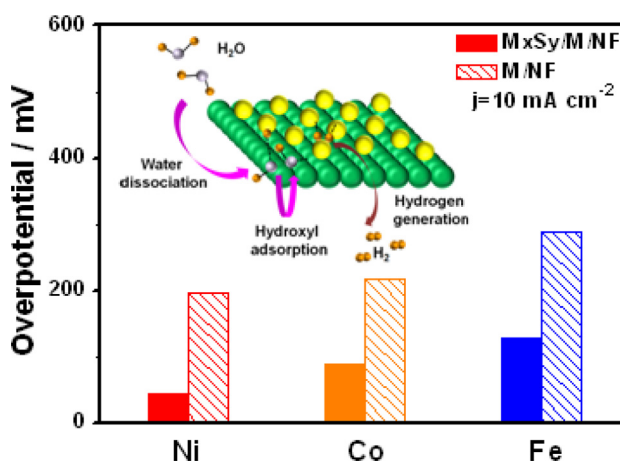
<sup>b</sup> Hangzhou Institute of Advanced Studies, Zhejiang Normal University, Hangzhou 311231, China

<sup>c</sup> Vacuum Interconnected Nanotech Workstation, Suzhou Institute of Nano-Tech and Nano-Bionics, Chinese Academy of Sciences, Suzhou 215123, China

## HIGHLIGHTS

- A general one-step electrodeposition method was used to construct metal surfaces decorated with metal sulfide nanoparticles.
- The decoration of metal sulfide nanoparticles induces an exceptional HER activity.
- A very low overpotential of 45 mV is required at  $10 \text{ mA cm}^{-2}$  for  $\text{Ni}_3\text{S}_2/\text{Ni}/\text{NF}$ .
- DFT calculations reveal the synergistic effect in the combination of metals and metal sulfides for boosted HER activity.

## GRAPHICAL ABSTRACT



## ARTICLE INFO

## Article history:

Received 13 August 2019

Revised 23 September 2019

Accepted 24 September 2019

Available online 25 September 2019

## Keywords:

One-step electrodeposition

Transition metal

Metal sulfide decoration

Hydrogen evolution reaction

DFT calculations

## ABSTRACT

Sluggish water dissociation kinetics in the Volmer step is still the huge challenge in designing and synthesizing transition-metal-based electrocatalysts for hydrogen evolution reaction (HER) in alkaline media. Herein, we report a general one-step electrodeposition strategy to construct a high-efficiency electrocatalytic system based on transition metals (Ni, Co and Fe) surface decorated with metal sulfide ( $\text{Ni}_3\text{S}_2$ ,  $\text{Co}_x\text{S}_y$  and  $\text{Fe}_x\text{S}_y$ ) nanoparticles on Ni foam with thiourea ( $\text{M}_x\text{S}_y/\text{M}/\text{NF}$ ). Evaluated in 1.0 M KOH, the obtained  $\text{Ni}_3\text{S}_2/\text{Ni}/\text{NF}$ ,  $\text{Co}_x\text{S}_y/\text{Co}/\text{NF}$  and  $\text{Fe}_x\text{S}_y/\text{Fe}/\text{NF}$  exhibit exceptionally enhanced HER activity, whose overpotentials at  $10 \text{ mA cm}^{-2}$  decrease from 196 to 45 mV, 217 to 89 mV and 288 to 128 mV, respectively, when metal sulfides are introduced to Ni/NF, Co/NF and Fe/NF electrodes. Compared with most of state-of-the-art transition-metal-based catalysts, the  $\text{Ni}_3\text{S}_2/\text{Ni}/\text{NF}$  electrode displays extremely low overpotential and small Tafel slope ( $54 \text{ mV dec}^{-1}$ ) as well as excellent stability. Further experimental characterizations and density functional theory calculations reveal that such excellent HER performance can be ascribed to the synergistic effect in the combination of metals and metal sulfides, the former of which enhances water dissociation and the latter accelerates hydrogen generation. This intriguing work opens a new avenue towards designing highly active low-cost electrocatalysts for commercial application.

© 2019 Elsevier Inc. All rights reserved.

\* Corresponding authors.

E-mail addresses: [yjzhong@zjnu.edu.cn](mailto:yjzhong@zjnu.edu.cn) (Y. Zhong), [yonghu@zjnu.edu.cn](mailto:yonghu@zjnu.edu.cn) (Y. Hu).

<sup>1</sup> These authors contributed equally to this work.

## 1. Introduction

As an environmentally friendly and renewable energy resource, hydrogen ( $H_2$ ) has been deemed an attractive alternative to conventional fossil fuels [1–3]. Among various  $H_2$  production pathways, electrocatalytic water splitting is an economical and promising approach to obtain  $H_2$  sustainably by utilizing renewable and abundant water resources [4,5]. However, the inevitable overpotential problem in the reaction process greatly limits the electrolysis efficiency [6,7]. The key to develop high-performance water splitting electrocatalysts is to accelerate the sluggish kinetics by reducing the overpotentials of hydrogen evolution reaction (HER) and oxygen evolution reaction (OER) [8,9]. Currently, noble-metal-based materials like Pt-based compounds are the state-of-the-art electrocatalysts for HER, but the low earth abundance and high-cost severely restrict their large-scale commercial application [10–13]. Therefore, it is rather urgent and crucial to develop earth-abundant and inexpensive catalysts with high HER activity [14].

Compared with acidic electrolytes, the electrocatalytic materials are more efficient and stable in alkaline electrolytes, and the development of electrocatalysts in alkaline electrolytes is more significant [11,15,16]. Actually, the HER process involves two steps in alkaline media. The first step is the water dissociation, the Volmer process, in which water is decomposed molecules into hydrogen intermediates ( $H_2O + e^- \rightarrow H_{ads} + OH^-$ ). The second step is the Heyrovsky process ( $H_{ads} + H_2O + e^- \rightarrow H_2 + OH^-$ ) or Tafel process ( $H_{ads} + H_{ads} \rightarrow H_2$ ), in which hydrogen intermediates are absorbed to produce  $H_2$  [17]. Obviously, the kinetics of HER in the alkaline media is determined by the balance between water decomposition and the subsequent  $H_2$  generation step [8,18]. Thus, it is vital for an efficient electrocatalyst to simultaneously possess a lower energy barrier for water dissociation and a faster rate for  $H_2$  generation [19,20].

Recent studies on various transition-metal-based compounds, such as phosphides [21–24], nitrides [25,26], carbides [27–30], sulfides [31–33], selenides [34,35] etc., have revealed excellent HER activity. Among various metal sulfides, nickel sulfide has aroused extensive attention due to its intrinsic metallic behaviors with high conductivity [36,37]. However, most single-component materials, with a single kind of active sites, exhibit poor electrocatalytic activity due to the inherent low capacity for  $H_2$  adsorption and desorption. Their intrinsic activity is only conducive to water dissociation or  $H_2$  generation step [38]. In this regard, constructing synergistic compounds is an efficient and promising strategy to improve HER performance, which can provide not only the active sites to decompose water molecules but also the active sites to produce  $H_2$  [14,38–40].

Herein, we report a general one-step electrodeposition strategy to construct transition-metal-based electrocatalysts decorated with metal sulfide nanoparticles on Ni foam ( $M_xS_y/M/NF$ ,  $M = Ni, Co, Fe$ ) with the presence of thiourea (TU). The as-prepared  $Ni_3S_2/Ni/NF$ ,  $Co_xS_y/Co/NF$  and  $Fe_xS_y/Fe/NF$  electrodes exhibit exceptionally enhanced activity for HER due to the decoration of corresponding metal sulfides, whose overpotentials decrease to 45 mV, 89 mV and 128 mV from 196 mV, 217 mV and 288 mV of their  $Ni/NF$ ,  $Co/NF$  and  $Fe/NF$  counterparts at  $10 \text{ mA cm}^{-2}$  in 1.0 M KOH, respectively. Further experimental characterizations and theoretical investigations reveal that the significantly enhanced performance profits from the synergy effects of the combined transition metals and metal sulfides, which both accelerates water dissociation and speeds up  $H_2$  generation.

## 2. Experimental section

### 2.1. Synthesis of $M_xS_y/M/NF$ ( $M = Ni, Co, Fe$ ) and $M/NF$

The  $Ni_3S_2/Ni/NF$  electrode was synthesized via a facile one-step electrodeposition. In a typical synthesis, a piece of commercial NF with a size of  $0.5 \text{ cm} \times 1.5 \text{ cm}$  was firstly immersed in 3 M HCl solution for 10 min to remove the superficial nickel oxides with the aid of an ultrasonic bath, and then washed with deionized water and ethanol for several times. The electrodeposition was carried out in a standard two-electrode system at room conditions with an electrolyte consisting of 0.1 M nickel acetate tetrahydrate ( $Ni(CH_3COO)_2 \cdot 4H_2O$ ), 2.0 M ammonium chloride ( $NH_4Cl$ ) and 0.1 M TU. The pretreated NF and a Pt wire were employed as the working electrode and the counter electrode, respectively. After the galvanostatic electrolysis at a current of  $-1.0 \text{ A cm}^{-2}$  for 400 s, the resulting working electrode was rinsed with a large amount of water and ethanol, and finally the  $Ni_3S_2/Ni/NF$  electrode material was obtained. The electrolytes containing different concentration of TU, including 0.05 M, 0.1 M and 0.2 M, were used to prepare the different  $Ni_3S_2/Ni/NF$  samples. In addition, the deposition time of 300 s, 400 s, and 500 s were applied for the electrodeposition of different  $Ni_3S_2/Ni/NF$  samples. Moreover, the same synthetic procedure was employed to prepare other transition metal surface decorated with metal sulfide nanoparticles on NF. 0.1 M cobalt acetate tetrahydrate ( $Co(CH_3COO)_2 \cdot 4H_2O$ ) or 0.1 M ferrous sulfate heptahydrate ( $FeSO_4 \cdot 7H_2O$ ) instead of 0.1 M  $Ni(CH_3COO)_2 \cdot 4H_2O$  was employed for the electrodeposition of the corresponding  $M_xS_y/M/NF$  ( $M = Co$  and  $Fe$ ) electrode at a constant current of  $-1.0 \text{ A cm}^{-2}$  for 400 s, respectively. The synthesis process of  $M/NF$  ( $M = Ni, Co, Fe$ ) is similar to that of  $M_xS_y/M/NF$  except for the absence of TU.

### 2.2. Synthesis of etched- $Ni_3S_2/Ni/NF$

The etched- $Ni_3S_2/Ni/NF$  was synthesized by a leaching method, in which the  $Ni_3S_2/Ni/NF$  sample was immersed in the 0.1 M disodium ethylenediamine tetraacetate ( $Na_2EDTA$ ) solution at 30 °C for 3 h, 5 h and 10 h, respectively. The sample was finally washed with deionized water and ethanol for several times.

### 2.3. Materials characterization

X-ray diffraction patterns (XRD) were acquired on a Philips PW3040/60 X-ray diffractometer using the  $Cu-K\alpha$  radiation at a scanning rate of  $0.06^\circ \text{ s}^{-1}$ . Scanning electron microscopy (SEM) measurements were conducted on a Hitachi S-4800 scanning electron microanalyzer with an accelerating voltage of 15 kV. Transmission electron microscopy (TEM) and high-resolution transmission electron microscopy (HRTEM) measurements were performed on a JEM-2100F field-emission TEM at 200 kV. X-ray photoelectron spectra (XPS) were measured on an ESCALab MKII X-ray photoelectron spectrometer with  $Mg K\alpha$  X-ray as the excitation source. XPS depth profiles were measured with an etching rate of  $0.97 \text{ nm s}^{-1}$  and etching area of  $1 \text{ mm} \times 1 \text{ mm}$ .

### 2.4. Electrochemical measurements

The electrochemical properties of the as-prepared catalysts toward hydrogen evolution reaction (HER) were performed on a computer-controlled CHI 660E electrochemical workstation with a three-electrode cell system in 1.0 M KOH aqueous solution ( $pH = 13.6$ ). Catalysts deposited on NF were directly employed as

the working electrodes, saturated calomel (SCE, saturated KCl) as a reference electrode and graphite rod as a counter electrode. All the potentials in this study were converted to the reversible hydrogen electrode (RHE) reference scale according to  $E_{(RHE)} = -E_{(SCE)} + 0.059 \text{ pH} + 0.241$ . The polarization curves were obtained through linear sweep voltammetry (LSV) with a scan rate of  $2 \text{ mV s}^{-1}$ . Electrochemical impedance spectroscopy (EIS) measurements were measured with the frequency range from 0.01 Hz to 100000 Hz. All the polarized curves obtained from LSV were corrected with 80% iR-compensation.

### 2.5. Computational methodology

Density functional theory (DFT) calculations were performed using Vienna ab initio Simulation Package (VASP) [41,42] based on the projected augmented wave (PAW) [43,44] method. Spin-polarized Perdew–Burke–Ernzerhof (PBE) exchange–correlation functional [45] has been employed to describe exchange and correlation interactions. A plane wave basis set with energy cut off of 400 eV and appropriate k-points were used to ensure the convergence of total ground-state energy. All geometrical optimization were performed until force acting on relaxing atoms was less than  $0.02 \text{ eV/Å}$ . Bulk Ni and  $\text{Ni}_3\text{S}_2$  have been optimized self-consistently, achieving  $a = 3.514 \text{ Å}$  (experimental:  $a = 3.524 \text{ Å}$ ) for Ni, and  $a = 5.728 \text{ Å}$  and  $c = 7.131 \text{ Å}$  (experimental:  $a = 5.640 \text{ Å}$ ,  $c = 7.132 \text{ Å}$ ) for  $\text{Ni}_3\text{S}_2$ . From HRTEM characterization, we have known that Ni (1 1 1) facets and  $\text{Ni}_3\text{S}_2$  (1 1 0) facets are dominant exposing morphologies for each phase, so we use them to model the corresponding HER. Ni (1 1 1) was modeled with a four layers slab of  $3 \times 3$  surface supercell.  $\text{Ni}_3\text{S}_2$  (1 1 0) was modeled with a four layers slab of  $1 \times 2$  surface supercell. Adsorption of the intermediates involved in HER in basic condition was investigated, and the binding energy was calculated via  $E_a(X) = E(X@Slab) - E(X) - E(Slab)$ . Various adsorption sites were test, and only the results at the most favorable sites are given. Chemical potential of  $\text{OH}^-/\text{H}_2\text{O}/\text{H}_2$  have been determined via the scheme proposed by Norskov et al. [46,47] and zero point energy has been included.

## 3. Results and discussion

As schematically illustrated in Fig. 1, a series of 3D broccoli-like  $\text{M}_x\text{S}_y/\text{M}/\text{NF}$  electrodes are designed and prepared as electrocatalysts for HER in alkaline media via one-step galvanostatic electrodeposition route, using different transition-metal salts, ammonium chloride ( $\text{NH}_4\text{Cl}$ ) and TU as starting reagents. The morphology of the as-prepared  $\text{Ni}_3\text{S}_2/\text{Ni}/\text{NF}$  electrode was first examined by the scanning electron microscopy (SEM) measurements. As shown in Fig. S1a and b, the pristine NF displays the smooth surface. After electrodeposition, the as-obtained  $\text{Ni}_3\text{S}_2/\text{Ni}/\text{NF}$  electrode (Fig. 2a) obviously exhibits the 3D broccoli-like morphology, which is composed by the accumulation of numerous nanoparticles on NF. Without the presence of TU, the morphology of the as-obtained Ni/NF electrode is almost the same as the  $\text{Ni}_3\text{S}_2/\text{Ni}/\text{NF}$  electrode (Fig. S1c and d), suggesting that the introduction of TU does not change the morphology of the final products in the electrodeposition process. Additionally, the as-prepared other  $\text{M}_x\text{S}_y/\text{M}/\text{NF}$  and M/NF ( $\text{M} = \text{Co}$  and  $\text{Fe}$ ) electrodes also exhibit the similar 3D broccoli-like morphology after one-step electrodeposition (Figs. S2 and S3).

Furthermore, detailed structural information of the  $\text{Ni}_3\text{S}_2/\text{Ni}/\text{NF}$  electrode is evaluated by the transmission electron microscopy (TEM) and selected area electron diffraction (SAED). Fig. 2b shows the TEM image of a small piece of  $\text{Ni}_3\text{S}_2/\text{Ni}$  sample exfoliated from the  $\text{Ni}_3\text{S}_2/\text{Ni}/\text{NF}$  by ultrasonic treatment, which also confirms that the broccoli-like structure of sample is composed of nanoparticles,

and this result is consistent with the SEM. As shown in Fig. 2c, the high-resolution TEM (HRTEM) image taken from the selected area of Fig. 2b shows two distinct lattice fringes. The set of  $0.20 \text{ nm}$  is consistent with the (1 1 1) plane of metallic Ni [48], and the other with a distance of  $0.29 \text{ nm}$  and an interplanar angle of  $60^\circ$  is assigned to the {1 1 0} plane of the hexagonal phase of  $\text{Ni}_3\text{S}_2$  [36]. Fig. 2d displays the SAED pattern of  $\text{Ni}_3\text{S}_2/\text{Ni}/\text{NF}$ , revealing the characteristic diffraction rings corresponding to metallic Ni (1 1 1), (2 0 0), (2 2 0), (3 1 1) [49] and hexagonal  $\text{Ni}_3\text{S}_2$  (1 0 1), (1 1 0), (0 2 1), (3 0 0) [36], respectively. Both the HRTEM and SAED results confirm that the as-prepared sample contains metallic Ni and  $\text{Ni}_3\text{S}_2$ . And the corresponding elemental mapping results of the  $\text{Ni}_3\text{S}_2/\text{Ni}/\text{NF}$  in Fig. 2e–g show the uniform distribution of Ni and S elements, further indicating the  $\text{Ni}_3\text{S}_2$  is successfully introduced by the addition of TU in the electrodeposition process.

The phase informations of the as-prepared  $\text{Ni}_3\text{S}_2/\text{Ni}/\text{NF}$  and Ni/NF electrodes was examined by X-ray diffraction (XRD) techniques, as shown in Fig. 3a. For Ni/NF, the three sharp diffraction peaks are indexed well to metallic Ni (JCPDS 04–0850). In the contrast, the  $\text{Ni}_3\text{S}_2/\text{Ni}/\text{NF}$  also exhibits only three weaker diffraction peaks analogous to Ni/NF without any additional peak, illustrating that the crystallinity of  $\text{Ni}_3\text{S}_2$  in  $\text{Ni}_3\text{S}_2/\text{Ni}/\text{NF}$  electrode is relatively poor. Additionally, the XRD results of the as-obtained  $\text{M}_x\text{S}_y/\text{M}/\text{NF}$  ( $\text{M} = \text{Co}$  and  $\text{Fe}$ ) electrodes mainly contain metallic Co (JCPDS 05–0727) and Fe (JCPDS 06–0696), respectively (Fig. S4). And the samples used for XRD test are exfoliated from  $\text{M}_x\text{S}_y/\text{M}/\text{NF}$  and M/NF by ultrasonic treatment to avoid the influence of the strong peaks of NF.

To further elucidate the surface states of the as-obtained  $\text{Ni}_3\text{S}_2/\text{Ni}/\text{NF}$  electrode, the X-ray photoelectron spectroscopy (XPS) measurements were also performed. As shown in Fig. 3b, the high-resolution spectra of Ni 2p exhibits two main peaks at  $855.8 \text{ eV}$  and  $873.5 \text{ eV}$ , which are assigned to Ni 2p<sub>3/2</sub> and Ni 2p<sub>1/2</sub> electronic configurations of  $\text{Ni}^{2+}$  in  $\text{Ni}_3\text{S}_2$ , with two satellite peaks at  $861.1 \text{ eV}$  and  $879.5 \text{ eV}$ , respectively [50,51]. And the two small peaks at  $852.6 \text{ eV}$  and  $869.8 \text{ eV}$  can be ascribed to metallic Ni [14,52]. Fig. 3c shows the XPS spectrum of S 2p and the peaks at  $162.4 \text{ eV}$  and  $163.6 \text{ eV}$  are attributable to S 2p<sub>3/2</sub> and S 2p<sub>1/2</sub>, respectively [50,53]. These results confirm the coexistence of Ni and  $\text{Ni}_3\text{S}_2$  in the final product as revealed by the HRTEM and SAED analyses. Moreover, to understand the chemical compositions of the as-obtained  $\text{Ni}_3\text{S}_2/\text{Ni}/\text{NF}$  electrode, XPS depth profiles are further carried out, as shown in Fig. 3d. With the increased etching time, the peaks of  $\text{Ni}^{2+}$  become weaker and weaker or even disappear, indicating that high valence Ni only exists on the surface of the sample, namely,  $\text{Ni}_3\text{S}_2$  nanoparticles are merely decorated on the surface of metallic Ni in the  $\text{Ni}_3\text{S}_2/\text{Ni}/\text{NF}$  system. And the content of Ni and S in the  $\text{Ni}_3\text{S}_2/\text{Ni}/\text{NF}$  from XPS results was listed in the Table S1. The ratio of Ni:S on the surface is about 3.4:1 (Table S1) which is larger than 3:2 of the pure  $\text{Ni}_3\text{S}_2$ , confirming that the abundance of metallic Ni and the limitation of  $\text{Ni}_3\text{S}_2$  on the surface of the as-prepared electrode. Additionally, the corresponding  $\text{M}_x\text{S}_y$  ( $\text{M} = \text{Co}$  and  $\text{Fe}$ ) in the as-prepared  $\text{M}_x\text{S}_y/\text{M}/\text{NF}$  electrodes are further testified by the XPS measurements. The results in Figs. S5 and S6 indicate the co-existence of the metallic Co and cobalt sulfide in  $\text{Co}_x\text{S}_y/\text{Co}/\text{NF}$  as well as the metallic Fe and ferrous sulfide in  $\text{Fe}_x\text{S}_y/\text{Fe}/\text{NF}$ . In a word, all SEM, XRD and XPS characterizations reveal that all samples ( $\text{M}_x\text{S}_y/\text{M}/\text{NF}$ ) formed by this electrodeposition method maintain the similar 3D broccoli-like morphology and chemical compositions.

According to the relevant literatures and above results, the probable electrodeposition mechanism is proposed as follows [54,55]. First,  $\text{M}^{n+}$  is easily reduced to transition-metal via Equation (Eq. (1)). Meanwhile, some  $\text{M}^{n+}$  ions can combine with TU to form  $\text{M}(\text{TU})^{n+}$  via Eq. (2), while the concentration of  $\text{M}^{n+}$  decreases due to the continuous reduction of  $\text{M}^{n+}$ , resulting in the increase of dis-

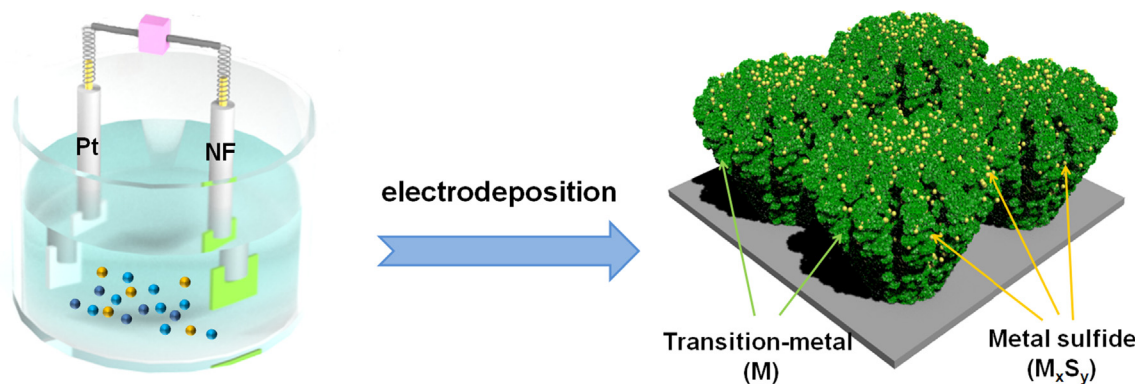


**Fig. 1.** Schematic illustration for the preparation of the  $M_xS_y/M/NF$  ( $M = Ni, Co$  and  $Fe$ ) electrocatalyst. Dark blue dots:  $NH_4Cl$ ; light blue dots: TU; orange dots: different transition- metal salts.

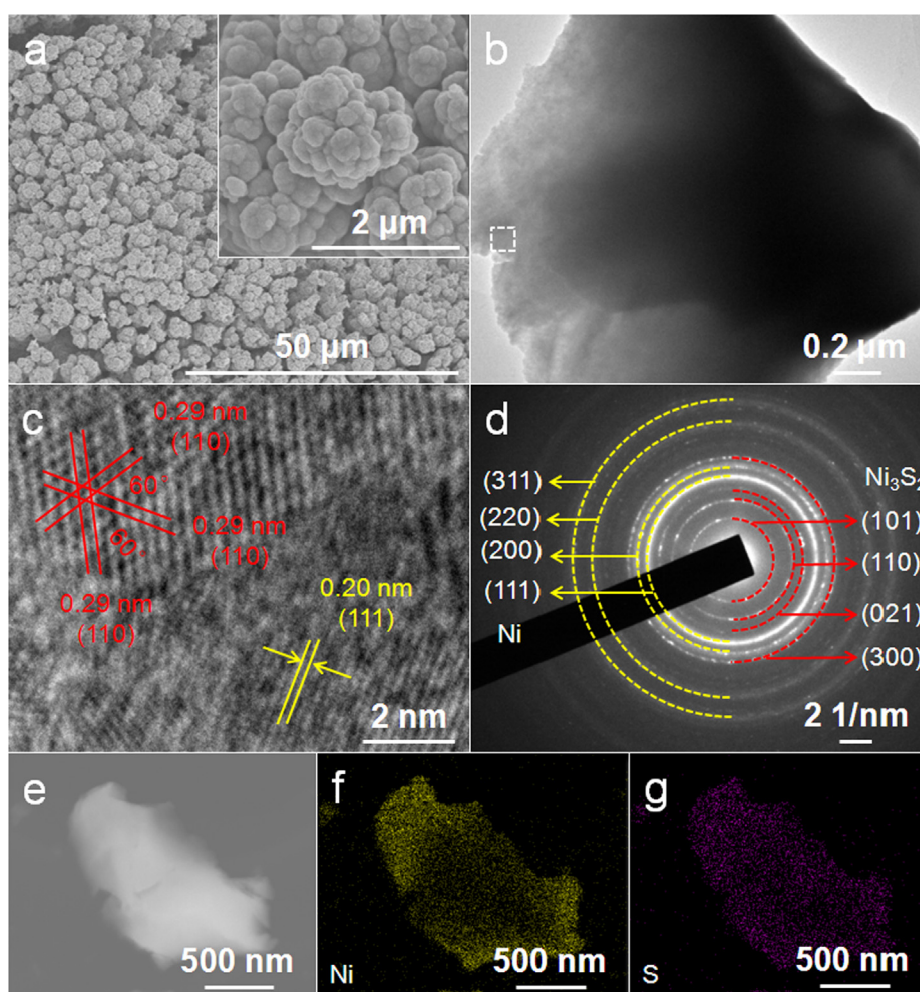
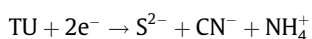
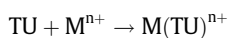
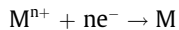


**Fig. 2.** (a) SEM images, (b) TEM image, (c) HRTEM image, (d) SAED pattern and (e) STEM image of the as-obtained  $Ni_3S_2/Ni/NF$ , and the corresponding elemental mapping images of (f) Ni and (g) S.

sociative TU. Then, the dissociative TU is decomposed to  $S^{2-}$  ions via Eq. (3) and further produce  $M_xS_y$  with metal via Eq. (4).



The HER catalytic property of the  $Ni_3S_2/Ni/NF$  electrode was investigated with linear sweep voltammetry at a scan rate of  $2 \text{ mV s}^{-1}$  in 1.0 M KOH solution with a standard three-electrode configuration. The effect of the different electrodeposition time and different TU concentration in the electrodeposition process on the HER performance of the final  $Ni_3S_2/Ni/NF$  electrode was first

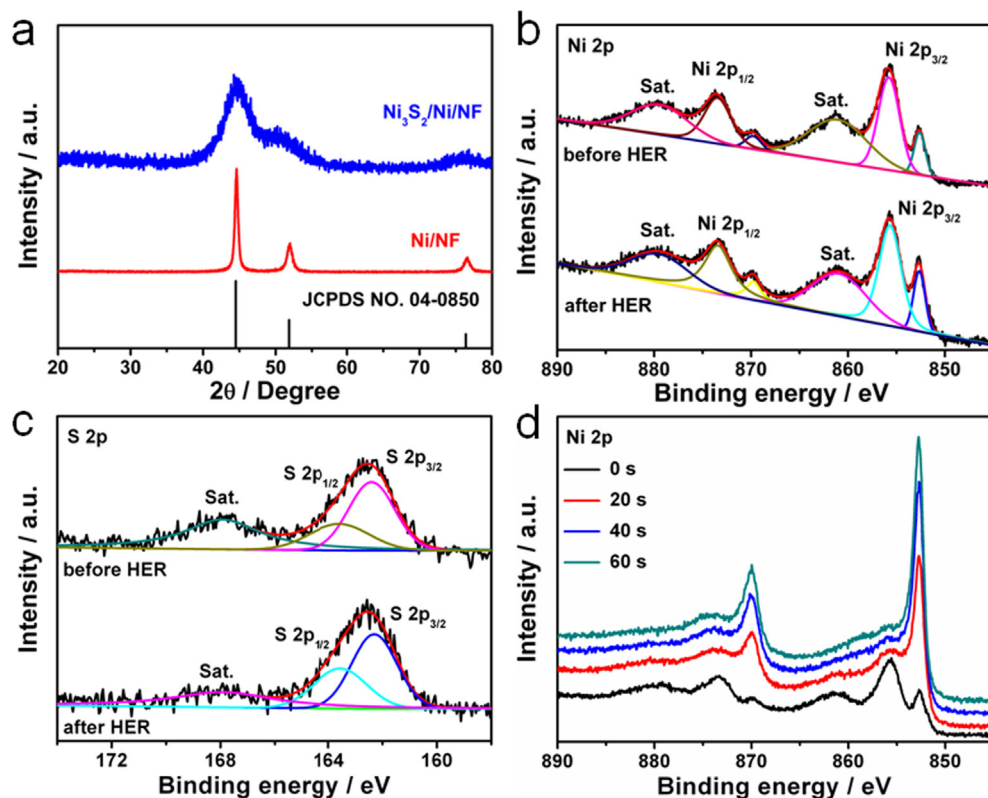


**Fig. 3.** (a) XRD patterns of  $\text{Ni}_3\text{S}_2/\text{Ni}/\text{NF}$  and  $\text{Ni}/\text{NF}$ . High-resolution XPS spectra of the  $\text{Ni}_3\text{S}_2/\text{Ni}/\text{NF}$  before and after HER test: (b) Ni 2p, (c) S 2p. (d) High-resolution Ni 2p XPS spectra of the  $\text{Ni}_3\text{S}_2/\text{Ni}/\text{NF}$  etched for different times.

carried out, as shown in Fig. S7. Apparently, an optimal  $\text{Ni}_3\text{S}_2/\text{Ni}/\text{NF}$  electrode with the best HER performance can be observed when the electrodeposition time for 400 s with the presence of 0.1 M TU. As a contrast, the corresponding  $\text{Ni}/\text{NF}$ , NF and Pt/C (20%) electrodes are also tested, as displayed in Fig. 4a. The overpotential of  $\text{Ni}_3\text{S}_2/\text{Ni}/\text{NF}$  electrode at the current density of  $10 \text{ mA cm}^{-2}$  is only 45 mV, which is close to 37 mV of the state-of-the-art commercial Pt/C and about 3 times and 4 times lower than 196 mV of  $\text{Ni}/\text{NF}$  and 258 mV of NF, respectively, confirming that decorating  $\text{Ni}_3\text{S}_2$  nanoparticles on the surface of Ni leads to a drastically enhancement of the HER performance. Besides, the HER performance of  $\text{Ni}_3\text{S}_2/\text{Ni}/\text{NF}$  is also superior to some recently reported transition-metal-based catalysts in Table S2 including NC-NiCu-NiCuN (93 mV) [56],  $\text{Ni}_2\text{P}/\text{Ni}/\text{NF}$  (98 mV) [57] and  $\text{NiO}/\text{Ni}-\text{CNT}$  (80 mV) [58]. Specifically in Fig. 4b, to achieve current density of  $100 \text{ mA cm}^{-2}$ ,  $\text{Ni}_3\text{S}_2/\text{Ni}/\text{NF}$  demands a small overpotential of 115 mV, which is 179 mV and 360 mV lower than 294 mV of  $\text{Ni}/\text{NF}$  and 475 mV of NF, respectively. It is worth mentioning that the activity of  $\text{Ni}_3\text{S}_2/\text{Ni}/\text{NF}$  is even superior to Pt/C at the large current density. Additionally, as expected, other  $\text{M}_x\text{S}_y/\text{M}/\text{NF}$  ( $\text{M} = \text{Co}$  and  $\text{Fe}$ ) samples with the decoration of metal sulfide show a greatly enhanced activity as well (Fig. S8). Fig. 4c clearly displays the performance comparison of a series of  $\text{M}_x\text{S}_y/\text{M}/\text{NF}$  and  $\text{M}/\text{NF}$ . In particular, the overpotentials at  $10 \text{ mA cm}^{-2}$  of  $\text{Ni}_3\text{S}_2/\text{Ni}/\text{NF}$ ,  $\text{Co}_x\text{S}_y/\text{Co}/\text{NF}$  and  $\text{Fe}_x\text{S}_y/\text{Fe}/\text{NF}$  decrease to 45 mV, 89 mV and 128 mV from 196 mV, 217 mV and 288 mV of  $\text{Ni}/\text{NF}$ ,  $\text{Co}/\text{NF}$  and  $\text{Fe}/\text{NF}$ , respectively. These results strongly prove the universality of our one-step electrodeposition engineering with the presence of TU to construct  $\text{M}_x\text{S}_y/\text{M}/\text{NF}$  and the enhanced HER performance via decorating metal sulfide on the transition-metal surface.

To verify the important role of  $\text{Ni}_3\text{S}_2$  in  $\text{Ni}_3\text{S}_2/\text{Ni}/\text{NF}$  in the increased HER performance, the etched- $\text{Ni}_3\text{S}_2/\text{Ni}/\text{NF}$  electrode was obtained via immersing  $\text{Ni}_3\text{S}_2/\text{Ni}/\text{NF}$  in the disodium ethylene-

diamine tetraacetate ( $\text{Na}_2\text{EDTA}$ ) solution which only reacts with  $\text{Ni}^{2+}$  instead of metallic Ni to etch away the  $\text{Ni}_3\text{S}_2$  on the surface. After  $\text{Na}_2\text{EDTA}$  treatment for 5 h, the sample (etched- $\text{Ni}_3\text{S}_2/\text{Ni}/\text{NF}$ -5) retains the 3D broccoli-like structure as shown in the Fig. S9. Fig. S10a in the supporting information shows polarization curves of the samples soaked in  $\text{Na}_2\text{EDTA}$  for different time. The HER property of  $\text{Ni}_3\text{S}_2/\text{Ni}/\text{NF}$  after soaking in  $\text{Na}_2\text{EDTA}$  for 5 h declines precipitously compared with the pristine one but basically remain unchanged with further prolonged time, indicating that the  $\text{Ni}_3\text{S}_2$  on the surface of the sample has been completely removed after 5 h. The etched- $\text{Ni}_3\text{S}_2/\text{Ni}/\text{NF}$ -5 electrode achieves an overpotential of 190 mV at  $10 \text{ mA cm}^{-2}$  with a Tafel slope of  $117 \text{ mV dec}^{-1}$  (Fig. S10b), which reduces sharply compared with  $\text{Ni}_3\text{S}_2/\text{Ni}/\text{NF}$  but is similar to the  $\text{Ni}/\text{NF}$ . Hence, it is undeniable that the  $\text{Ni}_3\text{S}_2$  nanoparticles on the surface of Ni have a remarkable influence on promoting HER performance in alkaline solution.

The improved activity of  $\text{Ni}_3\text{S}_2/\text{Ni}/\text{NF}$  can be further proved by corresponding Tafel slope. As shown in Fig. 4d, the Tafel slope of  $\text{Ni}_3\text{S}_2/\text{Ni}/\text{NF}$  electrode is only  $54 \text{ mV dec}^{-1}$ , which is lower than  $102 \text{ mV dec}^{-1}$  of  $\text{Ni}/\text{NF}$  and  $209 \text{ mV dec}^{-1}$  of NF, implying the better HER kinetic process of  $\text{Ni}_3\text{S}_2/\text{Ni}/\text{NF}$  electrode with introduced  $\text{Ni}_3\text{S}_2$ . This expedited kinetic process can be also confirmed by electrochemical impedance spectroscopy (EIS) measurements. The Nyquist plots of  $\text{Ni}_3\text{S}_2/\text{Ni}/\text{NF}$  and  $\text{Ni}/\text{NF}$  are fitted to an equivalent circuit in Fig. S11a together with a series corresponding EIS data including solvent resistance ( $R_s$ ), charge-transfer resistance ( $R_{ct}$ ) and constant phase-element (CPE). The smaller  $R_{ct}$  for  $\text{Ni}_3\text{S}_2/\text{Ni}/\text{NF}$  compared with  $\text{Ni}/\text{NF}$  in Fig. S11b further demonstrates the advantage of decorating  $\text{Ni}_3\text{S}_2$  which endows the sample with a faster charge-transfer capacity and thus promotes the HER process [59]. In addition, to obtain insight into the increased performance of  $\text{Ni}_3\text{S}_2/\text{Ni}/\text{NF}$ , the electrochemical double-layer capacitance ( $C_{dl}$ ) examination is investigated comparing with the  $\text{Ni}/\text{NF}$ . As the

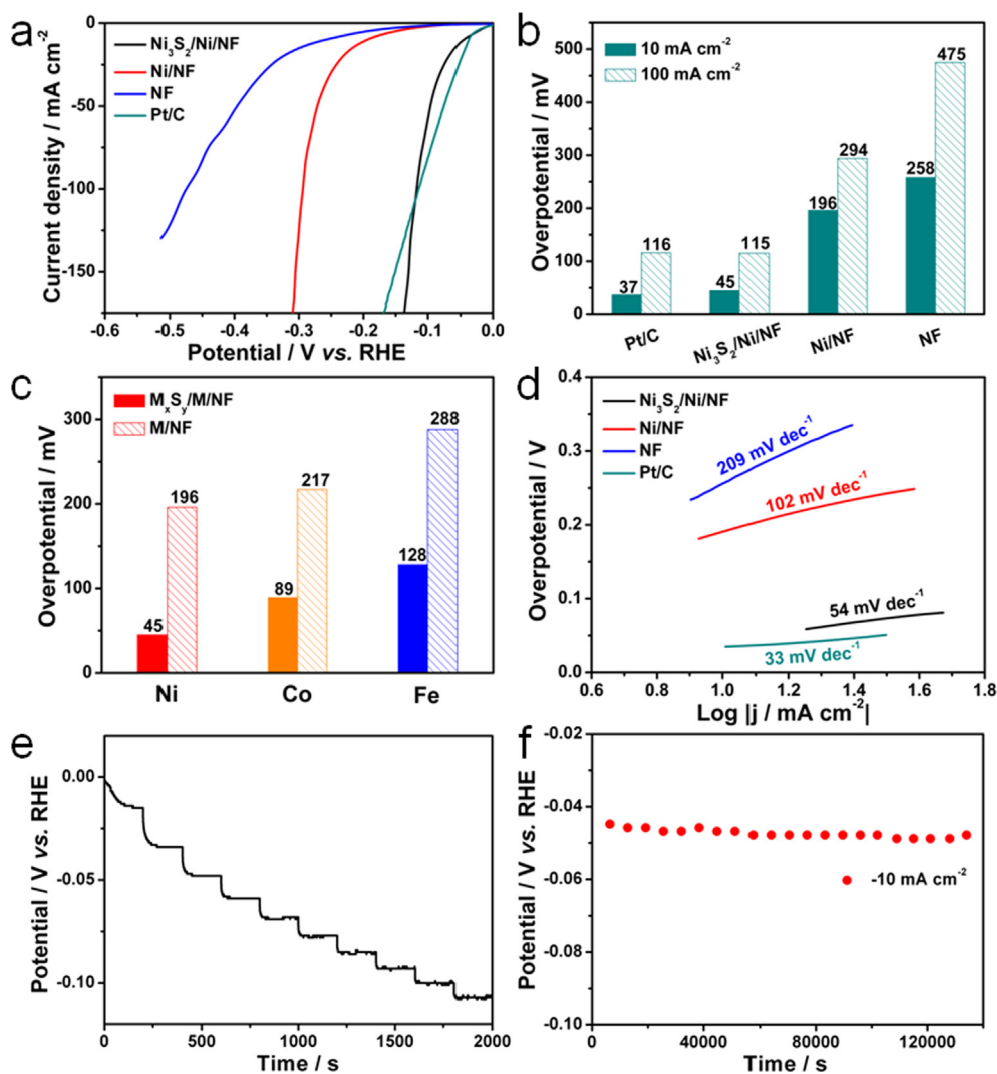


**Fig. 4.** (a) LSV curves and (b) overpotentials at 10 mA cm<sup>-2</sup> and 100 mA cm<sup>-2</sup> of the Ni<sub>3</sub>S<sub>2</sub>/Ni/NF, Ni/NF, NF and Pt/C in 1.0 M KOH solution for HER, (c) comparison of overpotentials at the current density of 10 mA cm<sup>-2</sup> for the M<sub>x</sub>S<sub>y</sub>/M/NF and M/NF (M = Ni, Co and Fe) electrodes, (d) tafel plots of the Ni<sub>3</sub>S<sub>2</sub>/Ni/NF, Ni/NF, NF and Pt/C, (e) multi-current process of the Ni<sub>3</sub>S<sub>2</sub>/Ni/NF, and the current density started at 2 mA cm<sup>-2</sup> and ended at 20 mA cm<sup>-2</sup> with an increment of 2 mA cm<sup>-2</sup> per 200 s. (f) Chronopotentiometric curve of the Ni<sub>3</sub>S<sub>2</sub>/Ni/NF electrode.

results shown in Fig. S12, the  $C_{dl}$  is 79.3 mF cm<sup>-2</sup> for Ni<sub>3</sub>S<sub>2</sub>/Ni/NF versus 52.9 mF cm<sup>-2</sup> for Ni/NF, indicating the Ni<sub>3</sub>S<sub>2</sub>/Ni/NF exhibits larger electrochemical active surface area, corresponding to its better HER performance.

Besides the efficient electrocatalytic performance, long-term stability is another criterion to evaluate a catalyst. The multi-step chronopotentiometric curve for Ni<sub>3</sub>S<sub>2</sub>/Ni/NF with cathodic current density increasing from 2 to 20 mA cm<sup>-2</sup> (an increment of 2 mA cm<sup>-2</sup> per 200 s) is shown in the Fig. 4e. The potential immediately levels off at the initial current value and remains unchanged for 200 s, and all other steps give the analogous results, illustrating the excellent mechanical robustness, conductivity and mass transportation of this electrocatalyst [60,61]. The chronopotentiometry result with current density of 10 mA cm<sup>-2</sup> is further performed in Fig. 4f, which exhibits no evident degradation after 140,000 s. And no obvious change can be observed from the polarization curves before and after the long-term stability test (Fig. S13), indicating the excellent HER catalytic stability of Ni<sub>3</sub>S<sub>2</sub>/Ni/NF. The morphology of the Ni<sub>3</sub>S<sub>2</sub>/Ni/NF electrode after stability test still remains the 3D broccoli-like structure examined by SEM (Fig. S14), indicating the good structural stability. Furthermore,

the Ni<sub>3</sub>S<sub>2</sub>/Ni/NF electrode after HER measurement was characterized by SEM, TEM and XPS. The morphology of the sample after HER (Fig. S15a and b) still remains the 3D broccoli-like structure, suggesting a strong mechanical robustness. Furthermore, the diffraction rings and lattice fringes of Ni and Ni<sub>3</sub>S<sub>2</sub> can be observed in SAED pattern (Fig. S15c) and HRTEM (Fig. S15d), respectively, revealing the coexistence of Ni and Ni<sub>3</sub>S<sub>2</sub> in the Ni<sub>3</sub>S<sub>2</sub>/Ni/NF after the HER measurements. And the results of XPS on the samples after HER test in Fig. 4b, c and Table S1 are similar to the pristine one, which illustrates that there is no change in the composition at the surface of the sample. All these results confirm the high stability of the Ni<sub>3</sub>S<sub>2</sub>/Ni/NF in alkaline solution.

In order to elucidate the exceptional HER performance of Ni<sub>3</sub>S<sub>2</sub>/Ni in alkaline solution, density functional theory (DFT) calculations were utilized to investigate whether the surface of Ni and Ni<sub>3</sub>S<sub>2</sub> could promote the water dissociation or H<sub>2</sub> generation. The adsorption configurations for HER intermediates H<sub>2</sub>O\*, \*OH and H\* on Ni and Ni<sub>3</sub>S<sub>2</sub> surfaces are shown in the Figs. S16 and S17. The standard free energy profiles from H<sub>2</sub>O molecule adsorption to H<sub>2</sub> desorption on Ni (1 1 1) and Ni<sub>3</sub>S<sub>2</sub> (1 1 0) surfaces are plotted in Fig. 5a. In consistency with previous DFT studies [62], the reac-

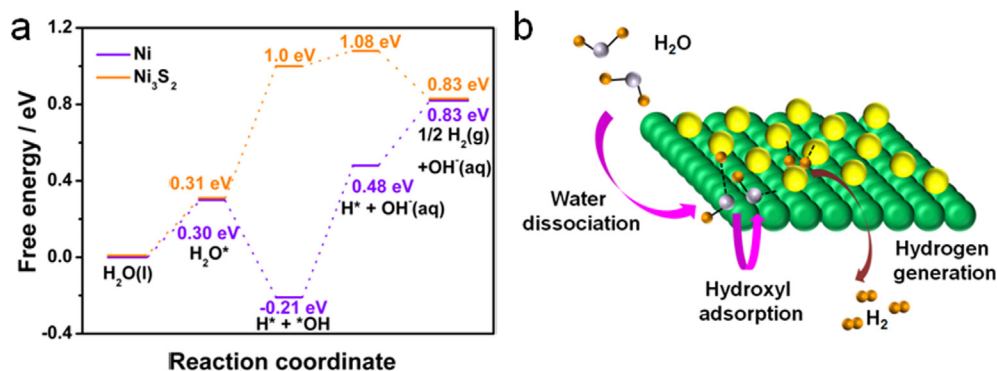


**Fig. 5.** (a) Free energy diagrams of HER on the Ni and Ni<sub>3</sub>S<sub>2</sub>. (b) Diagram showing HER catalytic reaction in Ni<sub>3</sub>S<sub>2</sub>/Ni/NF. Purple balls: O atoms; orange balls: H atoms; green balls: metallic Ni; yellow balls: Ni<sub>3</sub>S<sub>2</sub>.

tion free energy of H<sub>2</sub>O dissociation on Ni(1 1 1) is  $-0.51$  eV, which is much lower compared with that on Ni<sub>3</sub>S<sub>2</sub> (1 1 0) (0.69 eV). It shows that Ni (1 1 1) is much more favorable for H<sub>2</sub>O dissociation. However, on Ni (1 1 1), both \*OH and H\* intermediates are binding too strongly (as listed in Table S3) to proceed the following steps. In contrast, on Ni<sub>3</sub>S<sub>2</sub> (1 1 0), HER is hindered from the H<sub>2</sub>O dissociation due to weak binding of H\* and \*OH. Turning to the H<sub>2</sub> generation, the energy barrier of electron transfer for \*OH on Ni<sub>3</sub>S<sub>2</sub> (1 1 0) is particularly small and the adsorption of H\* on Ni<sub>3</sub>S<sub>2</sub> (1 1 0) is approaching thermal neutral referenced to H<sub>2</sub>, indicating that H\* formed on Ni<sub>3</sub>S<sub>2</sub> (1 1 0) is ready to desorb as H<sub>2</sub>. This implies that the Ni<sub>3</sub>S<sub>2</sub> could serve as a proper active phase for HER. When taken into consideration the Ni<sub>3</sub>S<sub>2</sub>/Ni/NF as integrated constitution, a more comprehensive HER process on Ni<sub>3</sub>S<sub>2</sub>/Ni/NF may exist (Fig. 5b): \*OH and H\* tend to be formed via water dissociation on Ni surfaces, and then transfer over Ni<sub>3</sub>S<sub>2</sub> for consequential steps, during which H<sub>2</sub> is formed and released from Ni<sub>3</sub>S<sub>2</sub>.

Combining the results of DFT calculations and experiment characterizations, the superior HER electrocatalytic activity of Ni<sub>3</sub>S<sub>2</sub>/Ni/NF can be attributed to the following aspects: (1) the metallic Ni in Ni<sub>3</sub>S<sub>2</sub>/Ni/NF efficiently breaks the O–H of absorbed H<sub>2</sub>O, promoting the water dissociation, (2) the Ni<sub>3</sub>S<sub>2</sub> possesses a thermal neutral binding strength of hydrogen atom, which is beneficial to the generation and release of H<sub>2</sub>, and (3) the direct electrodeposition of Ni<sub>3</sub>S<sub>2</sub>/Ni nanoparticles on the conductive NF without polymer binder reduces the shielding of the active sites and establishes the strong adhesion between Ni<sub>3</sub>S<sub>2</sub>/Ni and NF which is conducive to its electrocatalytic stability. Additionally, the excellent electrocatalytic activity of other M<sub>x</sub>S<sub>y</sub>/M/NF (M = Co and Fe) electrodes can also be ascribed to above merits.

#### 4. Conclusions

In summary, we have developed a general strategy to construct a high-efficiency electrocatalytic system based on transition-metal surfaces decorated with metal sulfide nanoparticles on NF (M<sub>x</sub>S<sub>y</sub>/M/NF, M = Ni, Co, Fe) via a facile one-step electrodeposition method. Impressively, the decoration of metal sulfide results in a significantly enhanced HER activity in 1.0 M KOH compared to those transition-metal catalysts (M/NF) without modification. Notably, among these M<sub>x</sub>S<sub>y</sub>/M/NF electrodes, Ni<sub>3</sub>S<sub>2</sub>/Ni/NF shows exceptional performance with low overpotential of 45 mV at 10 mA cm<sup>-2</sup> and excellent long-term durability. Experimental studies and DFT calculations disclose that the synergistic effect of the transition-metal and metal sulfides plays an important role in promoting the HER performance, establishing a balance between water dissociation and hydrogen generation. Our study records a facile and universal method to design advanced electrocatalysts for hydrogen evolution reaction under alkaline conditions.

#### Declaration of Competing Interest

The authors declared that there is no conflict of interest.

#### Acknowledgments

The authors acknowledge financial support from the Natural Science Foundation of China (21671173, 11504299) and Zhejiang Provincial Ten Thousand Talent Program (2017R52043).

#### Appendix A. Supplementary material

Supplementary data to this article can be found online at <https://doi.org/10.1016/j.jcis.2019.09.090>.

#### References

- [1] X. Zou, Y. Zhang, Noble metal-free hydrogen evolution catalysts for water splitting, *Chem. Soc. Rev.* 44 (2015) 5148–5180.
- [2] D. Zhang, H. Mou, F. Lu, C. Song, D. Wang, A novel strategy for 2D/2D NiS/graphene heterostructures as efficient bifunctional electrocatalysts for overall water splitting, *Appl. Catal. B: Environ.* 254 (2019) 471–478.
- [3] E. Hu, J. Ning, B. He, Z. Li, C. Zheng, Y. Zhong, Z. Zhang, Y. Hu, Unusual formation of tetragonal microstructures from nitrogen-doped carbon nanocapsules with cobalt nanocores as a bi-functional oxygen electrocatalyst, *J. Mater. Chem. A* 5 (2017) 2271–2279.
- [4] C. Lei, Y. Wang, Y. Hou, P. Liu, J. Yang, T. Zhang, X. Zhuang, M. Chen, B. Yang, L. Lei, C. Yuan, M. Qiu, X. Feng, Efficient alkaline hydrogen evolution on atomically dispersed Ni–N<sub>x</sub> species anchored porous carbon with embedded Ni nanoparticles by accelerating water dissociation kinetics, *Energy Environ. Sci.* 12 (2019) 149–156.
- [5] L. Wang, L. Ren, X. Wang, X. Feng, J. Zhou, B. Wang, Multivariate MOF-templated pomegranate-like Ni/C as efficient bifunctional electrocatalyst for hydrogen evolution and urea oxidation, *ACS Appl. Mater. Inter.* 10 (2018) 4750–4756.
- [6] L. Zeng, K. Sun, X. Wang, Y. Liu, Y. Pan, Z. Liu, D. Cao, Y. Song, S. Liu, C. Liu, Three-dimensional-networked Ni<sub>2</sub>P/Ni<sub>3</sub>S<sub>2</sub> heteronanoflake arrays for highly enhanced electrochemical overall-water-splitting activity, *Nano Energy* 51 (2018) 26–36.
- [7] H. Jiang, J. Gu, X. Zheng, M. Liu, X. Qiu, L. Wang, W. Li, Z. Chen, X. Ji, J. Li, Defect-rich and ultrathin N doped carbon nanosheets as advanced trifunctional metal-free electrocatalysts for the ORR, OER and HER, *Energy Environ. Sci.* 12 (2019) 322–333.
- [8] Q. Jin, B. Ren, D. Li, H. Cui, C. Wang, In situ promoting water dissociation kinetic of Co based electrocatalyst for unprecedentedly enhanced hydrogen evolution reaction in alkaline media, *Nano Energy* 49 (2018) 14–22.
- [9] E. Hu, Y. Feng, J. Nai, D. Zhao, Y. Hu, X.W. Lou, Construction of hierarchical Ni–Co–P hollow nanobricks with oriented nanosheets for efficient overall water splitting, *Energy Environ. Sci.* 11 (2018) 872–880.
- [10] J. Wang, W. Cui, Q. Liu, Z. Xing, A.M. Asiri, X. Sun, Recent progress in cobalt-based heterogeneous catalysts for electrochemical water splitting, *Adv. Mater.* 28 (2016) 215–230.
- [11] S.Q. Liu, H.R. Wen, G. Ying, Y.W. Zhu, X.Z. Fu, R. Sun, C.P. Wong, Amorphous Ni(OH)<sub>2</sub> encounter with crystalline CuS in hollow spheres: a mesoporous nano-shelled heterostructure for hydrogen evolution electrocatalysis, *Nano Energy* 44 (2018) 7–14.
- [12] P. Kuang, M. He, H. Zou, J. Yu, K. Fan, 0D/3D MoS<sub>2</sub>–NiS<sub>2</sub>/N-doped graphene foam composite for efficient overall water splitting, *Appl. Catal. B: Environ.* 254 (2019) 15–25.

- [13] E. Hu, X.-Y. Yu, F. Chen, Y. Wu, Y. Hu, X.W.D. Lou, Graphene layers-wrapped Fe/Fe<sub>3</sub>C<sub>2</sub> nanoparticles supported on N-doped graphene nanosheets for highly efficient oxygen reduction, *Adv. Energy Mater.* 8 (2018) 1702476.
- [14] Y.Y. Ma, Z.L. Lang, L.K. Yan, Y.H. Wang, H.Q. Tan, K. Feng, Y.J. Xia, J. Zhong, Y. Liu, Z.H. Kang, Y.G. Li, Highly efficient hydrogen evolution triggered by a multi-interfacial Ni/WC hybrid electrocatalyst, *Energy Environ. Sci.* 11 (2018) 2114–2123.
- [15] Y. Luo, X. Li, X. Cai, X. Zou, F. Kang, H.M. Cheng, B. Liu, Two-dimensional MoS<sub>2</sub> confined Co(OH)<sub>2</sub> electrocatalysts for hydrogen evolution in alkaline electrolytes, *ACS Nano* 12 (2018) 4565–4573.
- [16] Y. Feng, C. Xu, E. Hu, B. Xia, J. Ning, C. Zheng, Y. Zhong, Z. Zhang, Y. Hu, Construction of hierarchical FeP/Ni<sub>2</sub>P hollow nanospindles for efficient oxygen evolution, *J. Mater. Chem. A* 6 (2018) 14103–14111.
- [17] Z. Zhu, H. Yin, C.-T. He, M. Al-Mamun, P. Liu, L. Jiang, Y. Zhao, Y. Wang, H.-G. Yang, Z. Tang, D. Wang, X.-M. Chen, H. Zhao, Ultrathin transition metal dichalcogenide/3d metal hydroxide hybridized nanosheets to enhance hydrogen evolution activity, *Adv. Mater.* 30 (2018) 1801171.
- [18] N. Danilovic, R. Subbaraman, D. Strmcnik, K.-C. Chang, A.P. Paulikas, V.R. Stamenkovic, N.M. Markovic, Enhancing the alkaline hydrogen evolution reaction activity through the bifunctionality of Ni(OH)<sub>2</sub>/metal catalysts, *Angew. Chem. Int. Ed.* 51 (2012) 12495–12498.
- [19] T. Zhang, K. Yang, C. Wang, S. Li, Q. Zhang, J. Li, S. Li, S. Jia, J. Wang, L. Fu, Nanometric Ni<sub>3</sub>P<sub>4</sub> clusters nested on NiCo<sub>2</sub>O<sub>4</sub> for efficient hydrogen production via alkaline water electrolysis, *Adv. Energy Mater.* 8 (2018) 1801690.
- [20] R. Subbaraman, D. Tripkovic, K.-C. Chang, D. Strmcnik, A.P. Paulikas, P. Hirunsit, M. Chan, J. Greeley, V. Stamenkovic, N.M. Markovic, Trends in activity for the water electrolyser reactions on 3d M(Ni Co, Fe, Mn) hydr(oxy)oxide catalysts, *Nat. Mater.* 11 (2012) 550.
- [21] P.W. Menezes, C. Panda, S. Loos, F. Bunschei-Bruns, C. Walter, M. Schwarze, X. Deng, H. Dau, M. Driess, A structurally versatile nickel phosphite acting as a robust bifunctional electrocatalyst for overall water splitting, *Energy Environ. Sci.* 11 (2018) 1287–1298.
- [22] J.X. Feng, S.Y. Tong, Y.X. Tong, G.R. Li, Pt-like hydrogen evolution electrocatalysis on PANI/CoP hybrid nanowires by weakening the shackles of hydrogen ions on the surfaces of catalysts, *J. Am. Chem. Soc.* 140 (2018) 5118–5126.
- [23] L. Yan, Y. Sun, E. Hu, J. Ning, Y. Zhong, Z. Zhang, Y. Hu, Facile in-situ growth of Ni<sub>2</sub>P/Fe<sub>2</sub>P nanohybrids on Ni foam for highly efficient urea electrolysis, *J. Colloid Interf. Sci.* 541 (2019) 279–286.
- [24] Y. Shi, Y. Xu, S. Zhuo, J. Zhang, B. Zhang, Ni<sub>2</sub>P nanosheets/Ni foam composite electrode for long-lived and pH-tolerable electrochemical hydrogen generation, *ACS Appl. Mater. Interf.* 7 (2015) 2376–2384.
- [25] C. Ray, S.C. Lee, B. Jin, A. Kundu, J.H. Park, S. Chan Jun, Conceptual design of three-dimensional CoN/Ni<sub>3</sub>N-coupled nanograsses integrated on N-doped carbon to serve as efficient and robust water splitting electrocatalysts, *J. Mater. Chem. A* 6 (2018) 4466–4476.
- [26] B. Zhang, C. Xiao, S. Xie, J. Liang, X. Chen, Y. Tang, Iron-nickel nitride nanostructures in situ grown on surface-redox-etching nickel foam: efficient and ultrasustainable electrocatalysts for overall water splitting, *Chem. Mater.* 28 (2016) 6934–6941.
- [27] H.B. Wu, B.Y. Xia, L. Yu, X.Y. Yu, X.W. Lou, Porous molybdenum carbide nano-octahedrons synthesized via confined carburization in metal-organic frameworks for efficient hydrogen production, *Nat. Commun.* 6 (2015) 6512.
- [28] F.X. Ma, H.B. Wu, B.Y. Xia, C.Y. Xu, X.W. Lou, Hierarchical β-Mo<sub>2</sub>C nanotubes organized by ultrathin nanosheets as a highly efficient electrocatalyst for hydrogen production, *Angew. Chem. Int. Ed.* 127 (2015) 15615–15619.
- [29] M. Zhang, Q. Dai, H. Zheng, M. Chen, L. Dai, Novel MOF-derived Co@N-C bifunctional catalysts for highly efficient Zn-air batteries and water splitting, *Adv. Mater.* 30 (2018) 1705431.
- [30] L. Tao, M. Qiao, R. Jin, Y. Li, Z. Xiao, Y. Wang, N. Zhang, C. Xie, Q. He, D. Jiang, G. Yu, Y. Li, S. Wang, Bridging the surface charge and catalytic activity of a defective carbon electrocatalyst, *Angew. Chem. Int. Ed.* 58 (2019) 1019–1024.
- [31] J.X. Feng, J.Q. Wu, Y.X. Tong, G.R. Li, Efficient hydrogen evolution on Cu nanodots-decorated Ni<sub>3</sub>S<sub>2</sub> nanotubes by optimizing atomic hydrogen adsorption and desorption, *J. Am. Chem. Soc.* 140 (2018) 610–617.
- [32] Z. Qian, Y. Chen, Z. Tang, Z. Liu, X. Wang, Y. Tian, W. Gao, Hollow nanocages of Ni<sub>x</sub>Co<sub>1-x</sub>Se for efficient zinc-air batteries and overall water splitting, *Nano-Micro Lett.* 11 (2019) 28.
- [33] J. Xu, J. Rong, F. Qiu, Y. Zhu, K. Mao, Y. Fang, D. Yang, T. Zhang, Highly dispersive NiCo<sub>2</sub>S<sub>4</sub> nanoparticles anchored on nitrogen-doped carbon nanofibers for efficient hydrogen evolution reaction, *J. Colloid Interf. Sci.* 555 (2019) 294–303.
- [34] J.Y. Zhang, H. Wang, Y. Tian, Y. Yan, Q. Xue, T. He, H. Liu, C. Wang, Y. Chen, B.Y. Xia, Anodic hydrazine oxidation assists energy-efficient hydrogen evolution over a bifunctional cobalt perselenide nanosheet electrode, *Angew. Chem. Int. Ed.* 57 (2018) 7649–7653.
- [35] J. Li, Q. Zhou, C. Yuan, P. Cheng, X. Hu, W. Huang, X. Gao, X. Wang, M. Jin, R. Nötzel, G. Zhou, Z. Zhang, J. Liu, Direct growth of vertically aligned ReSe<sub>2</sub> nanosheets on conductive electrode for electro-catalytic hydrogen production, *J. Colloid Interf. Sci.* 553 (2019) 699–704.
- [36] G. Zhang, Y.S. Feng, W.T. Lu, D. He, C.Y. Wang, Y.-K. Li, X.Y. Wang, F.F. Cao, Enhanced catalysis of electrochemical overall water splitting in alkaline media by Fe doping in Ni<sub>3</sub>S<sub>2</sub> nanosheet arrays, *ACS Catal.* 8 (2018) 5431–5441.
- [37] L.-L. Feng, G. Yu, Y. Wu, G.-D. Li, H. Li, Y. Sun, T. Asefa, W. Chen, X. Zou, High-index faceted Ni<sub>3</sub>S<sub>2</sub> nanosheet arrays as highly active and ultrastable electrocatalysts for water splitting, *J. Am. Chem. Soc.* 137 (2015) 14023–14026.
- [38] H. Jin, X. Liu, Y. Jiao, A. Vasileff, Y. Zheng, S.-Z. Qiao, Constructing tunable dual active sites on two-dimensional C<sub>3</sub>N<sub>4</sub>@MoN hybrid for electrocatalytic hydrogen evolution, *Nano Energy* 53 (2018) 690–697.
- [39] M. Zang, N. Xu, G. Cao, Z. Chen, J. Cui, L. Gan, H. Dai, X. Yang, P. Wang, Cobalt molybdenum oxide derived high-performance electrocatalyst for the hydrogen evolution reaction, *ACS Catal.* 8 (2018) 5062–5069.
- [40] Z.W. Seh, J. Kibsgaard, C.F. Dickens, I. Chorkendorff, J.K. Nørskov, T.F. Jaramillo, Combining theory and experiment in electrocatalysis: Insights into materials design, *Science* 355 (2017), eaad4998.
- [41] G. Kresse, J. Hafner, Ab initio molecular-dynamics simulation of the liquid-metal–amorphous-semiconductor transition in germanium, *Phys. Rev. B* 49 (1994) 14251–14269.
- [42] G. Kresse, J. Furthmüller, Efficiency of ab-initio total energy calculations for metals and semiconductors using a plane-wave basis set, *Comp. Mater. Sci.* 6 (1996) 15–50.
- [43] P.E. Blöchl, Projector augmented-wave method, *Phys. Rev. B* 50 (1994) 17953–17979.
- [44] G. Kresse, D. Joubert, From ultrasoft pseudopotentials to the projector augmented-wave method, *Phys. Rev. B* 59 (1999) 1758–1775.
- [45] J.P. Perdew, K. Burke, M. Ernzerhof, Generalized gradient approximation made simple, *Phys. Rev. Lett.* 77 (1996) 3865–3868.
- [46] H.-Y. Su, Y. Gorlin, I.C. Man, F. Calle-Vallejo, J.K. Nørskov, T.F. Jaramillo, J. Rossmeisl, Identifying active surface phases for metal oxide electrocatalysts: a study of manganese oxide bi-functional catalysts for oxygen reduction and water oxidation catalysis, *PCCP* 14 (2012) 14010.
- [47] M. Bajdich, M. García-Mota, A. Vojvodic, J.K. Nørskov, A.T. Bell, Theoretical investigation of the activity of cobalt oxides for the electrochemical oxidation of water, *J. Am. Chem. Soc.* 135 (2013) 13521–13530.
- [48] B. You, X. Liu, G. Hu, S. Gul, J. Yano, D.e. Jiang, Y. Sun, Universal surface engineering of transition metals for superior electrocatalytic hydrogen evolution in neutral water, *J. Am. Chem. Soc.* 139 (2017) 12283–12290.
- [49] Z. Zhuang, S.A. Giles, J. Zheng, G.R. Jenness, S. Caratzoulas, D.G. Vlachos, Y. Yan, Nickel supported on nitrogen-doped carbon nanotubes as hydrogen oxidation reaction catalyst in alkaline electrolyte, *Nat. Commun.* 7 (2016) 10141.
- [50] P. Chen, T. Zhou, M. Zhang, Y. Tong, C. Zhong, N. Zhang, L. Zhang, C. Wu, Y. Xie, 3D nitrogen-anion-decorated nickel sulfides for highly efficient overall water splitting, *Adv. Mater.* 29 (2017) 1701584.
- [51] S. Deng, K. Zhang, D. Xie, Y. Zhang, Y. Zhang, Y. Wang, J. Wu, X. Wang, H.J. Fan, X. Xia, J. Tu, High-index-faceted Ni<sub>3</sub>S<sub>2</sub> branch arrays as bifunctional electrocatalysts for efficient water splitting, *Nano-Micro Lett.* 11 (2019) 12.
- [52] S. Wang, J. Wang, M. Zhu, X. Bao, B. Xiao, D. Su, H. Li, Y. Wang, Molybdenum-carbide-modified nitrogen-doped carbon vesicles as encapsulating nickel nanoparticles: a highly efficient, low-cost catalyst for hydrogen evolution reaction, *J. Am. Chem. Soc.* 137 (2015) 15753–15759.
- [53] Y. Xiong, L. Xu, C. Jin, Q. Sun, Interface-engineered atomically thin Ni<sub>3</sub>S<sub>2</sub>/MnO<sub>2</sub> heterogeneous nanoarrays for efficient overall water splitting in alkaline media, *Appl. Catal. B: Environ.* 254 (2019) 329–338.
- [54] C.W. Su, J.M. Li, W. Yang, J.M. Guo, Electrodeposition of Ni<sub>3</sub>S<sub>2</sub>/Ni composites as high-performance cathodes for lithium batteries, *J. Phys. Chem. C* 118 (2013) 767–773.
- [55] J.Y. Lin, J.H. Liao, S.W. Chou, Cathodic electrodeposition of highly porous cobalt sulfide counter electrodes for dye-sensitized solar cells, *Electrochim. Acta* 56 (2011) 8818–8826.
- [56] J. Hou, Y. Sun, Z. Li, B. Zhang, S. Cao, Y. Wu, Z. Gao, L. Sun, Electrical behavior and electron transfer modulation of nickel-copper nanoalloys confined in nickel-copper nitrides nanowires array encapsulated in nitrogen-doped carbon framework as robust bifunctional electrocatalyst for overall water splitting, *Adv. Funct. Mater.* 28 (2018) 1803278.
- [57] B. You, N. Jiang, M. Sheng, M.W. Bhushan, Y. Sun, Hierarchically porous urchin-like Ni<sub>2</sub>P superstructures supported on nickel foam as efficient bifunctional electrocatalysts for overall water splitting, *ACS Catal.* 6 (2015) 714–721.
- [58] M. Gong, W. Zhou, M.C. Tsai, J. Zhou, M. Guan, M.C. Lin, B. Zhang, Y. Hu, D.Y. Wang, J. Wang, S.J. Pennycook, B.J. Hwang, H. Dai, Nanoscale nickel oxide/nickel heterostructures for active hydrogen evolution electrocatalysis, *Nat. Commun.* 5 (2014) 4695.
- [59] E. Hu, J. Ning, D. Zhao, C. Xu, Y. Lin, Y. Zhong, Z. Zhang, Y. Wang, Y. Hu, A room-temperature postsynthetic ligand exchange strategy to construct mesoporous Fe-doped CoP hollow triangle plate arrays for efficient electrocatalytic water splitting, *Small* 14 (2018) 1704233.
- [60] Z. Wu, X. Wang, J. Huang, F. Gao, A Co-doped Ni–Fe mixed oxide mesoporous nanosheet array with low overpotential and high stability towards overall water splitting, *J. Mater. Chem. A* 6 (2018) 167–178.
- [61] Z. Wang, X. Ren, X. Shi, Abdullah M. Asiri, L. Wang, X. Li, X. Sun, Q. Zhang, H. Wang, A platinum oxide decorated amorphous cobalt oxide hydroxide nanosheet array towards alkaline hydrogen evolution, *J. Mater. Chem. A* 6 (2018) 3864–3868.
- [62] M. Pozzo, G. Carlini, R. Rosei, D. Alfè, Comparative study of water dissociation on Rh(111) and Ni(111) studied with first principles calculations, *J. Chem. Phys.* 126 (2007) 164706.